Acta Materialia 196 (2020) 776–789

Contents lists available at ScienceDirect

Acta Materialia

journal homepage: www.elsevier.com/locate/actamat

Full length article

Creating, probing and confirming tetragonality in bulk FeNi alloys

N. Maât[a,c,1], I. McDonald[a,b,2], R. Barua[a,c,3], B. Lejeune[a,c], X. Zhang[b], G.M. Stephen[d,4], A. Fisher[b], D. Heiman[d], I.V. Soldatov[e,f], R. Schäfer[e,g], L.H. Lewis[a,b,c,*]

[a] Department of Chemical Engineering, Northeastern University, Boston, MA, United States
[b] Department of Mechanical and Industrial Engineering, Northeastern University, Boston, MA, United States
[c] George J. Kostas Research Institute for Homeland Security, Northeastern University, Boston, MA, United States
[d] Department of Physics, Northeastern University, Boston, MA, United States
[e] Leibniz Institute for Solid State and Materials Research (IFW) Dresden, Helmholtzstrasse 20, D-01069 Dresden, Germany
[f] Ural Federal University, Institute of Natural Sciences and Mathematics, 620002 Yekaterinburg, Russia
[g] Institute for Materials Science, TU Dresden, D-01062, Dresden, Germany

ARTICLE INFO

Article history:
Received 30 October 2019
Revised 15 June 2020
Accepted 5 July 2020
Available online 9 July 2020

ABSTRACT

Effects derived from the simultaneous application of passive, uniform saturating magnetic field and tensile stress during long-time annealing utilizing a unique and simple processing tool, the MultiDriver furnace, are reported. In particular, the evolution of the crystalline structure and the magnetic domain configuration of severely deformed and subsequently annealed equiatomic FeNi alloys were revealed by high-energy synchrotron X-Ray diffraction and Magneto-Optic Kerr Microscopy. These alloys are known to undergo a first-order magnetic phase transformation to a chemically ordered tetragonal ($L1_0$) structure in astronomical timeframes. MultiDriver-annealed specimens are found to retain a tetragonal crystallographic state and texture that is similar to that of the precursor deformed state, with a smaller unit cell volume and a larger c/a ratio relative to those of control samples that were annealed under the same conditions but without magnetic field and stress drivers. Magnetic domain images echo these observations: while as-cast FeNi alloys exhibit domain patterns consistent with the presence of a stress-modified cubic magnetocrystalline anisotropy, large areas of domains with uniaxial anisotropy are present in MultiDriver-annealed samples. While no chemical order was demonstrated in these samples, a strategy is proposed for achieving the ordered state by employing a passive magnetic gradient in the MultiDriver furnace to enhance diffusion.

1. Introduction

The control of phase selection and formation for targeted functionalities underpins the discipline of Materials Science. In most cases, this goal employs post-solidification (bulk) or post-deposition (film) processing conducted empirically through the application of a single intensive parameter, the temperature T, to produce a target daughter phase from a parent phase; there is much scope to improve this approach. Here we present results derived from application of a new and unique tool, the MultiDriver furnace [1], used to process bulk FeNi-based alloys that are precursors to the tetragonal FeNi phase — tetrataenite — with the chemically ordered $L1_0$ (prototype AuCu-I) structure. In this work, focus is directed towards processing of magnetic alloys in their bulk form because not only do bulk alloys provide the large magnetic flux density necessary for energy-related applications, such processing is entirely compatible with existing manufacturing infrastructure.

Comprised exclusively of easily accessible, abundant and non-toxic elements, the prospect of developing tetrataenite as a “gap” permanent magnet, with a maximum energy product that is between the weaker oxide ferrites and the stronger rare-earth magnets, continues to intrigue and engage magneticians around the world. Previous work conducted by Lewis and coworkers investigated tetrataenite derived from the NWA 6259 meteorite to quantify its technical magnetic properties [2,3,4,5,6,7,8]. From this work, it was concluded that tetrataenite has a theoretical maximum energy product at room temperature that is two-thirds of that of the

---

[*] Corresponding author at: Department of Chemical Engineering, Northeastern University, Boston, MA, United States.

E-mail address: lhlewis@northeastern.edu (L.H. Lewis).

[1] Current address: Eramet Ideas, 1 Avenue Albert Einstein, 78190 Trappes, France.

[2] Current address: EAG Laboratories, 810 Kifer Rd, Sunnyvale, CA 94086, United States.

[3] Current address: Virginia Commonwealth University, College of Engineering, 601 West Main Street, Box 843068, Richmond, VA 23284-3068, United States.

[4] Current address: Laboratory for Physical Sciences, 8050 Greenmead Drive, College Park, MD 20740, United States.

https://doi.org/10.1016/j.actamat.2020.07.019
1359-6454/

best NdFeB magnets [8]. However, the sluggish ordering kinetics to form the chemically ordered structure of tetrataenite require astronomical timescales for its meteoritic formation in nature. Addressing this issue, the MultiDriver Furnace is designed to allow application of simultaneous stress and magnetic driving forces for controlling phase transformation in bulk materials during thermal treatment. In this manner phase selection and arrangement can be tailored, and ideally accelerated, through management of multiple driving forces for phase formation. Indeed, employing results derived from high-energy synchrotron X-ray diffraction and Magneto-optic Kerr Effect (MOKE) microscopy, we demonstrate here the unequivocal attainment of magnetically uniaxiality in MultiDriver-processed FeNi alloys, indicating processing-induced tetragonality that is anticipated to foster chemical ordering to realize tetrataenite in bulk form and on earthly timescales.

1.1. Influencing thermodynamics and kinetics of phase transitions

Across all classes of functional materials, magnetic materials are most sensitive to very small and highly subtle aspects of the crystal and defect structure, composition and microstructure. In particular, the origins of intrinsic magnetic properties, such as saturation magnetization, Curie temperature and magnetocrystalline anisotropy energy are found in the quantum mechanical exchange interaction that is operative at the sub-nanometer atomic level. While this sensitivity gives rise to considerable challenges in materials design, it also provides great opportunity for the rational control of synthesis and processing to realize new and/or inaccessible magnetofunctional materials. It is known that many magnetofunctional systems feature strong coupling between the crystal lattice and the magnetic order, allowing perturbation of one aspect to influence the other [9–12]. Transcending the prevalent Edisonian approach, the effects of various free energy contributions to phase selection may be evaluated through examination of the total Gibbs Free Energy $G_{V,tot}$:

$$G_{V,tot} = (T \cdot S) + G_{magnetostatic} + G_{exchange} + G_{elastic} + G_{pressure} + G_{surface} + \cdots_{\ldots} \quad (1)$$

with T and S defined as temperature and entropy and including additional, self-explanatory Gibbs free contributions that are anticipated to influence magnetic transitions. The ground state of the system is determined by the overall free energy minimum governed by a balance of relevant energy terms in Eq. (1), and a phase transformation is triggered when the equivalence of the total free Gibb's energies of two competing phases is disrupted. Eq. (1) implies that phase equilibria in magnetoresponsive materials will be affected by the application of temperature, magnetic and/or pressure/stress fields, or appropriate combinations thereof. External applied fields are expected to impact phase transitions if the parent and daughter phases possess different field-conjugate properties [13,14]. For example, pressure/stress application is documented to strongly influence phase transformations that involve large volumetric changes [15,16,17,18]. The nucleation rate of ferromagnetic ferritic steel emerging from isothermal treatment of paramagnetic austenitic steel is reported to be increased by magnetic field application, allowing directed modification of the nose of associated T-T-T (time-temperature-transformation) diagrams [19,20]. A particularly complete history of the effects of magnetic fields on structure and response of iron and structural steels is provided in reference [21] and citations contained therein.

1.2. Phase transformations in equiatomic FeNi

The tetragonal $L1_0$ structure of tetrataenite forms in nominally equiatomic AB compounds from a chemically disordered, face centered cubic (fcc, A1) parent phase. It consists of alternating layers of the two constituent elements stacked in a direction parallel to the tetragonal *c*-axis, creating a natural superlattice that fosters a strong magnetocrystalline anisotropy in ferromagnetic systems [22–24]. This structure is known to crystallize along three variants, one for each of the three orthogonal crystallographic directions. While ferromagnetic $L1_0$-type systems typically possess a tetragonality, as described by the axial c/a ratio, that is less than unity, the c/a ratio of tetrataenite is greater than unity, albeit only slightly, with a reported $c/a = 1.0036$ [25]. Tetrataenite is thermodynamically more stable than typical fcc-type FeNi alloys but is found naturally only in stony, stony-iron, and iron meteorites that have been subjected to extremely slow cooling rates (0.2–10,000 kelvins per 10^6 years) [26]. This extraordinarily slow formation rate is attributed to i) a low driving force for chemical ordering, with the equilibrium order-disorder temperature reported as $T_{OD} = 320$ °C [27]; ii) the ferromagnetic character of its constituent atoms [28], and iii) to the intrinsically sluggish nature of nickel diffusion within an iron matrix [29]. While bulk synthesis of tetrataenite is widely considered to be technologically disruptive [30,31,32], to date no effort has been successful in developing this compound for permanent magnet applications. Nonetheless, a significant advance regarding tetrataenite synthesis was reported by Lewis and coworkers [7] using high-resolution neutron diffraction data performed on a series of highly strained and annealed samples of isotopically modified $Fe^{62}Ni$. Neutron diffraction on isotopically modified samples provides clear data, not obtainable with other probes, concerning the presence or absence of a superstructure in this compound. These studies concluded that specific processing protocols unequivocally produce a tetragonal – but not chemically ordered – phase in the FeNi system. These findings allowed the deduction that the A1-$L1_0$ phase transformation in FeNi occurs in two distinct steps: Step 1 is a stress-induced martensitic transformation from the A1 structure to the tetragonal chemically disordered phase with the A6 Strukturbericht designation structure (Pearson symbol tI2, Indium prototype structure) and Step 2 is a nucleation/diffusional process that produces the chemically ordered $L1_0$ phase from the tetragonal chemically disordered A6 phase. Experimental evidence indicates that the order-disorder phase transformation in $L1_0$ FeNi is thermodynamically of first order, in the Ehrenfest sense: experiments conducted on tetratatenite derived from NWA 6259 have documented the evolution of large latent heat of transformation [8], confirming that the transformation occurs by a nucleation and growth mechanism. These conclusions agree with those of Vlasova et al. who identified the A6 structure as a transitional phase in $L1_0$-type FePd [33]. Further, it implies that fostering an increased diffusion rate will promote the desired chemical order and associated increased magnetocrystalline anisotropy within the A6 structure.

2. The MultiDriver furnace

Specifically developed to influence phase selection in magnetic materials, the MultiDriver furnace [1] combines the two processing parameters of mechanical stress σ and magnetic field $\mu_0 H$ to thermally treat materials in a variety of atmospheres for extended periods of time. These drivers may be applied individually or simultaneously, employing a passive saturating magnetic field of close to 1 T. Typically, specialized metallurgical furnaces allow application of either stress/pressure or magnetic field during annealing, but not both. Historic and existing magnetic field-annealing furnaces employ superconducting magnets, electromagnets, or sometimes complex permanent magnet arrays [34,35]. However, the effectiveness of these furnaces is highly impeded by the active (*i.e.*, powered) operating mode of the magnet and/or the large air gap separating the sample from the magnet, reducing the magnetic flux delivered to the sample. The key feature of the MultiDriver

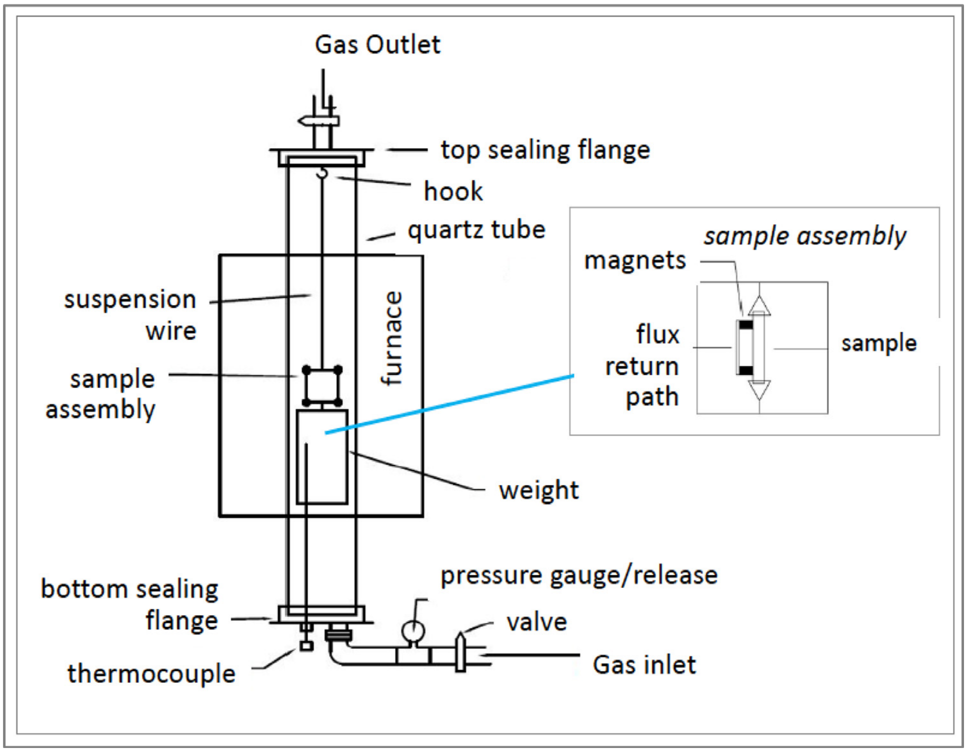

Fig. 1. Schematic diagram of the MultiDriver Furnace. Details concerning the components are provided in the text.

furnace, shown in Fig. 1, is the incorporation of a zero-gap/closed magnetic field circuit that applies a saturating magnetic field derived from a permanent magnet pair and minimizes demagnetization. The furnace equipment employed in this current study consists of a vertical tube furnace (MTI Corporation GSL-1100X) that is equipped with a 2-in. inner-diameter quartz tube that is sealed on both ends by a set of flanges to prevent oxidization and ambient contamination. The bottom flange includes two ports, one port for the insertion of a thermocouple to accurately monitor the real-time temperature and the second port for a gas inlet (preceded by a pressure release valve). The top flange includes a gas outlet as well as two small rings that are welded onto the inside surface of the flange for hanging or securing samples. The furnace set-up includes a roughing mechanical vacuum pump and a flowmeter. A tensile stress is administered by hanging a cylindrical weight from the suspended sample; two horizontal slots have been machined into the top and bottom of the samples to accommodate clips that suspend the weights and produce a uniform stress across the sample. Depending upon the cross-sectional area of the sample, stress values in excess of 10 MPa (0.1 kBar) may be delivered. The magnetic field is applied by attaching two permanent magnets to either end of the samples; the magnetic circuit was completed with a Mu-metal return path (see sample assembly inset of Fig. 1). The desired annealing temperature may be matched with the Curie temperature of the magnets. This unique magnetic field design largely eliminates inefficient magnetic fringing effects and, importantly, obviates demagnetization fields by guiding the magnetic field directly through the sample to provide magnetic saturation (for sample coercivity $H_{ci} < J_{sat}$, where J_{sat} is the saturation magnetization). In this manner the need for extremely high applied magnetic fields is circumvented. The estimated magnetic induction delivered to the sample was determined from a model (Ansys Electromagnetics software v. 17.2) of the magnetic circuit comprised of the FeNi sample clipped to SmCo magnets created. Simulation results (not published) for this configuration returned an approximate applied magnetic field value of 0.7 T available to magnetize the sample at elevated temperature.

3. Materials and methods

3.1. Overview

In this work, results obtained from FeNi alloys modified with additions of molybdenum are reported. The 5*d* transition metal Mo was chosen as an alloying addition by virtue of its optimized combination of cost, atomic radius and atomic number. Mo is anticipated to foster tetragonality in FeNi and to increase magnetocrystalline anisotropy by virtue of its approximately 10% larger atomic radius relative to Fe and Ni and its higher atomic number Z, respectively. As discussed by Du et al. [36] and citations contained therein, transition metals can exhibit an appreciable spin-orbit coupling which typically varies as Z^4. Data are reported from an alloy of nominal atomic composition $Fe_{49}Ni_{49}Mo_2$ as well as from an alloy of nominal equiatomic FeNi. As a first-order assumption, the physical and thermodynamic properties of these two compositions are the same, allowing direct comparison of results. After synthesis and homogenization, high-strain processing of these alloys was conducted by cold rolling to produce a highly defective starting material with a convenient annealing furnace geometry. Samples were heat-treated both in the absence of external stress and magnetic fields and in the presence of external stress and magnetic fields in the MultiDriver Furnace. After thermal treatment, surfaces of the samples parallel to the applied magnetic and strain fields were probed by high-energy synchrotron X-ray diffraction (XRD) and by Magneto-Optical Kerr Effect (MOKE) microscopy to examine the effects of processing.

3.2. Sample synthesis and processing

Ingots of nominal composition $(FeNi)_{98}Mo_2$ (also referred to as FeNi(Mo) in this work) were prepared from the elements (Alpha Aesar: Fe = 99.98%, Ni = 99.995%, Mo = 99.95%) by arc melting in Ar. After remelting each individual ingot five times to ensure chemical homogeneity, chemical composition of the samples was confirmed using field emission scanning electron microscopy

Table 1
Composition of $(FeNi)_{98}Mo_2$ sample as determined by EDS.

Nominal composition	at% Fe	at% Ni	at% Mo
$(FeNi)_{98}Mo_2$	52 ± 0.5	47 ± 0.5	1 ± 0.5

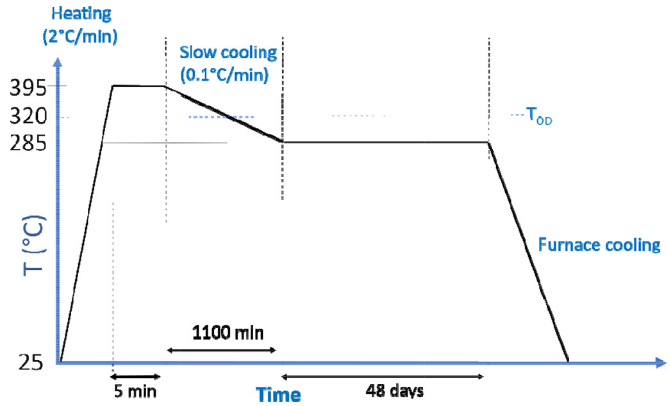

Fig. 2. Depiction of heat-treatment protocol applied to the cold-rolled FeNi(Mo) specimens. The same heat-treatment protocol is used both for conventional (CNTRL) annealing and for applied stress/magnetic field (CRFSA) annealing.

(FE-SEM, Hitachi S-4800) equipped with energy dispersive spectroscopy (EDS; EDAX). Five regions were probed for each sample with an error in composition estimated as ± 0.5 at%, with the determined elemental concentrations reported in Table 1.

Severe plastic deformation is expected to have a positive effect on atomic diffusion toward promoting phase transitions due to the creation of a high density of lattice defects [37,38], particularly dislocations that can serve as a source of abundant lattice vacancies [39,40]. To achieve the severely deformed state, cold rolling was conducted at the Ames Laboratory Materials Preparatory Center (MPC) [41] on single coalesced ingots to achieve a strain level ($\Delta t/t$, where t is the initial specimen thickness) of approximately 93%. The cold-rolling process was performed gradually in 13 steps, preserving the same rolling direction for each rolling pass. After rolling, the deformed specimens had dimensions of approximately 1 cm x 7 cm x 0.3 mm. These strips were then mounted on the sample assembly for annealing under the two conditions: conventional annealing with no stress or magnetic field applied (the control sample, denoted “CNTRL”) and annealing under simultaneous action of applied stress and magnetic field (the cold-rolled field- and stress-annealed sample, denoted “CRFSA”). The MultiDriver furnace was operated in small positive pressure (~3 psi) and steady flowrate (~0.1 L/min) of ultra-high purity Nitrogen gas (99.999%). Care was taken to ensure that the applied stress and magnetic field were applied in the same direction, along the rolling direction of the samples. As $L1_0$ FeNi possesses a c/a ratio > 1.0, this orientation was anticipated to promote favorably oriented crystallographic and microstructural changes under these drivers.

The heat treatment protocol used to process both the CNTRL and the CRFSA samples is diagrammed in Fig. 2. Samples were heated at 2 K/min to $T = 395$ °C, above the reported 320 °C order-disorder temperature of $L1_0$ FeNi, held for 5 min, then slowly cooled through T_{OD} to ~285 °C at −0.1 K/min and held for 48 days before furnace cooling to room temperature. This heat treatment protocol was based on that used by Tanaka and coworkers who demonstrated achievement of a monovariant $L1_0$-type structure in FePd by magnetic field annealing, or by applying a compressive stress during annealing [42,43]. A passive magnetic field was created in the MultiDriver Furnace through a magnetic circuit comprised of two small (~5 mm x 5 mm x 10 mm) axially magnetized commercial SmCo magnets (McMaster-Carr) and an electrical steel flux return path. A tensile stress of ~6.2 MPa was applied by hanging a cylindrical steel weight of 5.3 kg from the sample. Following annealing, representative samples were cut from the center of each strip using a low-speed diamond saw and polished by hand to remove a slight oxidation layer.

3.3. Crystal structure characterization using synchrotron X-ray diffraction

The extremely small tetragonal distortion ($c/a = 1.0036$) associated with the $L1_0$ phase of FeNi produces only very minor Bragg peak splitting that is highly challenging to detect as it is beneath the resolution limit of most laboratory-based X-ray diffraction (XRD) equipment. Furthermore, the intensity of XRD superstructure Bragg peaks produced by chemical ordering is also well below the detectable limit of laboratory XRD equipment. Indeed, the intensity of the (001) superlattice Bragg peak of $L1_0$-type FeNi is calculated to be only on the order of 0.3% of that of the strongest fundamental Bragg reflection, under the assumption of perfect chemical order. To address these issues, the lattice structure of these FeNi-based alloys was probed using high-resolution, high-energy synchrotron powder diffraction at the Advanced Photon Source (APS) Beamline 33-BM at the Argonne National Laboratory. Beamline 33-BM employs a sagittally focused double-crystal Si monochromator to achieve world-class sensitivity and resolution [44,45]. This configuration allows highly accurate measurement of lattice constants to within one standard deviation uncertainty of 0.0001 Å [46].

Diffraction data were collected at room temperature in the reflection mode (Bragg-Brentano geometry) for four FeNi(Mo) samples in the processing states described in Table 2: as-cast (AS), cold-rolled or deformed (CR), deformed and conventionally annealed (CNTRL) and deformed and MultiDriver Furnace-annealed (CRFSA). A radiation energy of 20 keV was selected to yield an X-ray wavelength of 0.619926 Å. Several locations near the center of each specimen were examined using an approximate beam area of 0.5 mm^2; the penetration depth of the X-rays, and hence the probe volume, was well in excess of 50 micrometers. In this manner it was possible to probe the bulk region of the material located below any deformed layer produced by mechanical polishing. Diffraction data were refined using the Rietveld method [47] and within the GSAS-II program [48], employing both cubic and tetragonal models. Parameters refined included the background signal, sample displacement, unit cell parameters, instrument parameters and crystallographic texture. At the end of the refinement, all parameters were allowed to vary simultaneously to convergence.

3.4. Surface topography, magnetic domain characterization using wide-field MOKE microscopy and magnetometry

Microscopic examination of the topographic surface conditions was accompanied by characterization of the magnetic domain configurations of the samples using wide-field Magneto-Optic Kerr Effect (MOKE) microscopy [49,50]. MOKE images can be captured during the application of a magnetic field, thus permitting the magnetization process to be followed. By measuring the integrated image intensity on selected sample spots during a full field sweep and plotting the result versus the applied field, MOKE magnetization loops can be obtained at the same time [51]. In case of bulk specimens, one must be aware that MOKE microscopy is a surface characterization technique, probing the magnetization up to 20 nm in depth in case of metallic materials [52]. Consequently, only the surface domains that are also responsible for the measured MOKE loops may be observed. As surface domains may significantly differ from the underlying volume domains [48], it is necessary to act with caution regarding interpretation of magnetic domains and

Table 2
FeNi(Mo) sample processing details, designations and descriptions.

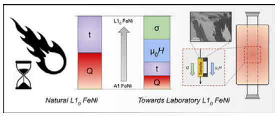

Sample condition	Designation	Experimental details
As-cast	AS	cast and homogenized
Cold-rolled	CR	degree of cold-worked strain ~93%
Cold-rolled and conventionally annealed: *Control sample*	CNTRL	annealed 48 days at 285 °C
Cold-rolled and field-stress annealed	CRFSA	annealed 48 days at 285 °C under the simultaneous influence of stress and magnetic field

loops. Furthermore, sample surface preparation is of utmost importance. Particular attention must be paid to the polishing procedure to avoid creation of a strained surface layer that damages and distorts the surface magnetic domain configuration [53–55]. Previous results (unpublished) indicate that the surface magnetic domain configuration of these FeNi-based samples is surprisingly susceptible to the polishing procedure, often exhibiting complex, uniaxial out-of-plane domain patterns (similar to those shown in Ref. [54]) that are actually polishing artifacts. In this current work, samples were mounted in ethanol-resistant wax and initially roughly polished with using a Struers RotoPol-31 Lab Grinder/Polisher. Fine polishing was performed by hand with various grades of SiC paper, and finally with MD Chem polishing cloths. The cloths were prepared with lubricant, ethanol and Buehler MasterMet 2 colloidal silica suspension. Such suspensions, which combine some chemical and mechanical polishing effects, are known from silicon wafer technology. For the preparation of magnetic materials, they were firstly applied to oxide magnets [56] but proved to be suitable also for stress-free polishing of metallic magnetic specimens [48]. All sample rinses were done with ethanol, and water was never used on the sample. The samples were dried with air. The polishing process took up to six hours per sample, and the progress of polishing was monitored by intermediate MOKE imaging to ascertain the quality of the surface and of the associated magnetic domains.

Once polishing was complete, the magnetic domains were imaged in a wide-field Kerr microscope using two objective lenses. Initially a 20x lens was used with a numerical aperture of 0.5. While this lens provides a lateral resolution of just 500 nm, it is suitable for capturing the domains in several grains within one image thus obtaining an overview of the magnetic domain configuration in a certain grain neighborhood. Subsequently an oil-immersed 100x lens with a numerical aperture of 1.3 was employed to see details of the domains at a highest resolution of about 220 nm. Captured MOKE data may be processed to yield difference images, in which an image of the magnetically saturated (i.e. domain-free) state is subtracted as a background image from the images containing magnetic contrast. The contrast in the difference images is free of topographic information and can be enhanced by digital image processing techniques. By combining images that are obtained at opposite directions of oblique light incidence in proper ways, it is possible to run the Kerr microscope under conditions of pure sensitivity to either perpendicular or to in-plane magnetization components [57], known as polar and longitudinal Kerr effect, respectively.

4. Results and analyses

4.1. Sample condition, crystallographic texture and lattice character

After prolonged MultiDriver furnace annealing, the samples' surfaces were only slightly oxidized and required minimal recleaning prior to examination with synchrotron XRD. Each X-ray diffraction data set indicates the presence of very well-crystallized samples with little or no secondary phases; these data are representative of those obtained from multiple regions in each sample. While a detailed analysis of the crystallographic texture of these samples is beyond the scope of this current study [58], nevertheless it is possible to extract useful information concerning the effects of MultiDriver processing of this alloy. The crystallographic textures of FeNi(Mo) specimens are found to exhibit marked differences associated with their processing state (as-cast (AS), cold-rolled (CR), conventionally annealed (CNTRL) and MultiDriver-annealed (CRFSA)). This aspect is evidenced by deviations of Bragg peak intensity from those of the ideal isotropic state, Fig. 3. This figure includes simulated reference Bragg peaks for the $Fe_{50}Ni_{50}$ composition with the A1 (fcc) structure, for comparison; tetragonal Miller indice peak labels are included in Fig. 3. Diffraction data obtained from the as-cast specimen, Fig. 3 (top left), show enhanced (111) and (220) peak intensities attributed to directional solidification effects that produced columnar grains along the thermal gradient direction. Attainment of (220) texture in FeNi materials has also been reported for Ni and for FeNi nanowire arrays [59–62]. The cold-rolled specimen shows the presence of a very strong (220) Bragg peak that dominates all other peaks in the XRD pattern, Fig. 3 (bottom left). This result is consistent with attainment of the well-known Goss texture found in Fe-based alloys upon deformation by rolling and recrystallization annealing [63,64]. The appreciable (111) Bragg peak intensity in the CR sample is attributed to grains with the (111) orientation that were initially present in the AS sample and were not completely eradicated by cold rolling.

The XRD patterns obtained from the two post-deformation annealing states are very different from one another. The conventionally annealed CNTRL sample (Fig. 3 (top right)) presents a strong (200) texture that is attributed to recrystallization of the strained precursor during long-term annealing. In contrast, the CRFSA sample subjected to MultiDriver furnace annealing retains a very intense (220) Bragg reflection (Fig. 3 (bottom right)), again exhibiting a strong texture that looks very much like that present in the same sample after cold rolling (Fig. 3 (bottom left)). In specific, it is concluded that application of stress and magnetic field drivers during post-deformation annealing prevents texture development along the (200) direction and promotes texture along the (220) direction. This observation strongly suggests that MultiDriver processing performed on these strained alloy precursors allows retention of the original deformed (CR) texture.

The effects of processing on the crystal lattice of samples in this study are revealed with the high-resolution data obtained from the APS synchrotron using high-energy, high-X-ray flux conditions. In particular, for all FeNi(Mo) samples examined in this work, structural refinements resulting from application of a tetragonal model to the XRD data were found to be unambiguously better across all goodness-of-fit parameters [65] than those returned from the refinement using the cubic model. Table 3 provides a summary of the lattice parameters and the weighted profile R-factors (R_{wp}) re-

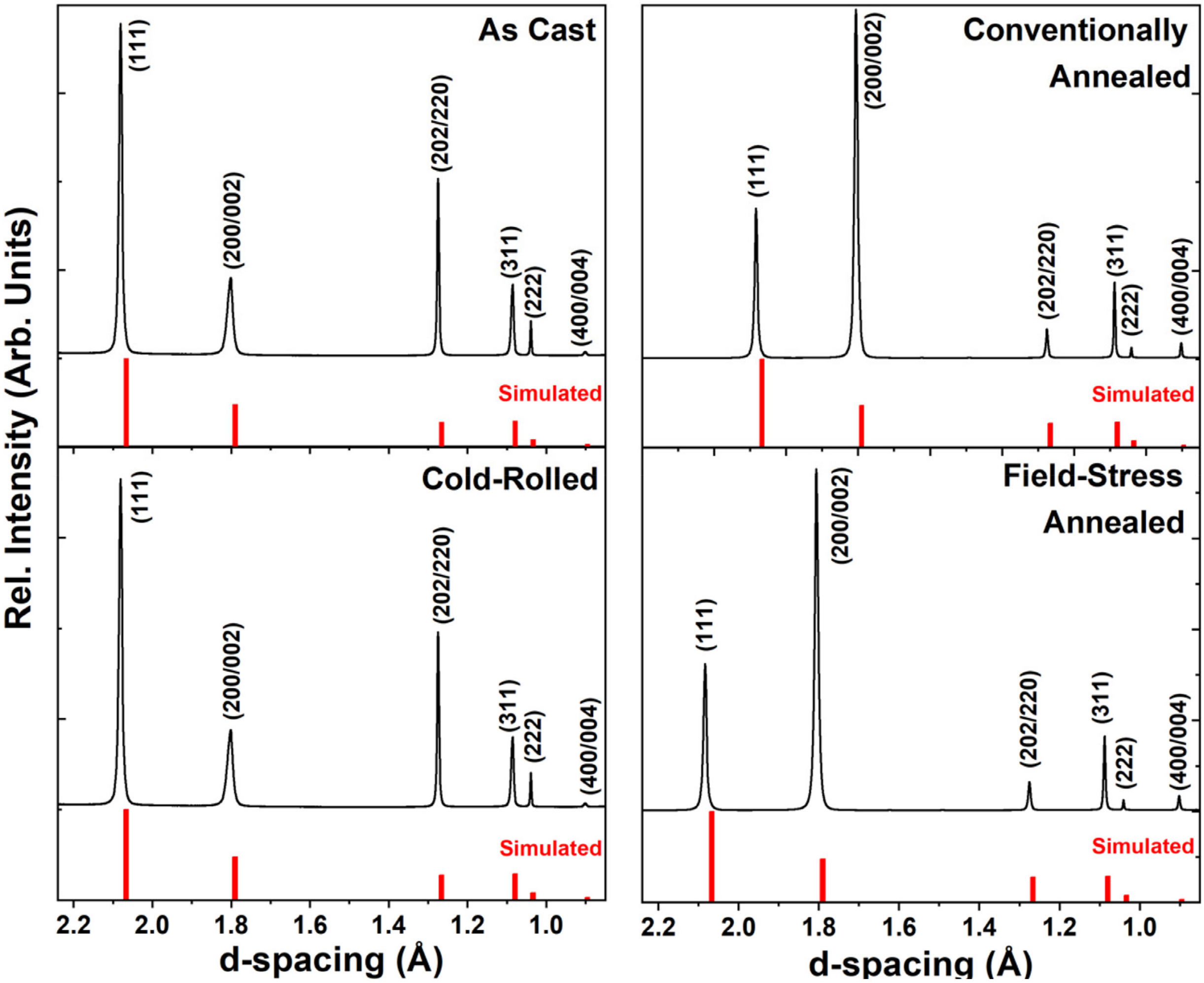

Fig. 3. Experimental and reference X-ray diffraction patterns of the $(FeNi)_{98}Mo_2$ samples, with Miller indices presented for a tetragonal structure. (top left): As-Cast (AS); (bottom left): Cold-Rolled (CR); (top right): Control (CNTRL) after conventional annealing; (bottom right): MultiDriver Furnace Field-Stress Annealed (CRFSA). The simulated XRD pattern for the cubic A1-type $Fe_{50}Ni_{50}$ phase with λ=0.619926 Å is displayed below each pattern.

Table 3

Comparison of Rietveld refinement-derived goodness-of-fit parameters and lattice parameters (including errors) of the $(FeNi)_{98}Mo_2$ samples resulting from application of a tetragonal model vs. a cubic model to the XRD data. Previously reported lattice parameters for as-cast equiatomic FeNi and for meteoritic $L1_0$ FeNi are included for comparison.

	FeNi(Mo) AS		FeNi(Mo) CR		FeNi(Mo) CNTRL		FeNi(Mo) CRFSA		FeNi AS [7]	$L1_0$ FeNi[25]
	Cubic	Tetrag.	Cubic	Tetrag.	Cubic	Tetrag.	Cubic	Tetrag.		
R_{wp}	14.9	10.4	17.6	14.3	15.4	7.9	14.8	7.7		
a-parameter ±0.0005 (Å)	3.6041	3.5952	3.6002	3.5824	3.6199	3.6045	3.5976	3.5879	3.58593	3.5761
c-parameter ±0.0005 (Å)		3.6101		3.6018		3.6138		3.5983	3.58722	3.5890
Unit cell volume ±0.02 ($Å^3$)	46.82	46.66	46.66	46.22	47.43	46.95	46.56	46.32	46.13	45.89
c/*a* ratio (±0.0003)		1.0041		1.0054		1.0022		1.0029	1.00036	1.0036

sulting from fits of the diffraction data to a cubic model and to a tetragonal model. It can be seen that R_{wp} is consistently smaller for data returned from the tetragonal fit. For comparison, also included in Table 3 are previously reported lattice parameters for as-solidified, homogenized equiatomic FeNi and for $L1_0$ FeNi derived from tetrataenite. Based on these results, going forward only tetragonal refined lattice parameters are presented and analyzed, using the values provided in Table 3. It can be noted that all cases the lattice parameters are smaller for the nominally binary FeNi specimen than for those with the Mo alloying addition. The as-cast FeNi(Mo) sample unit cell volume of 46.67 (±0.002) $Å^3$ is approximately 1.2% larger than that reported for $Fe_{50}Ni_{50}$ by Wakelin and Yates; this value is consistent with the presence of Mo in the lattice as well as with the noted Fe enrichment in our samples [66–70].

The data of Table 3 are presented in Fig. 4 which displays both the *c*/*a* ratios and the deviations in unit cell volume of the FeNi(Mo) samples relative to parameters of $L1_0$-type FeNi, as a function of the sample processing state. Upon deformation from the as-cast state, the degree of tetragonality, as quantified by the *c*/*a* ratio, increases, ranging from a low value of 1.00036 (±0.0003) (essentially cubic) for the as-cast sample to a high value of 1.0054 (±0.0003) for the cold-rolled sample. Simultaneously, the unit cell volume decreases by approximately 1%, from 46.67 $Å^3$ to 46.22 $Å^3$ (±0.002 $Å^3$), consistent with the introduction of a high density of lattice defects [71,6,72]. The subsequent differences in the lattice

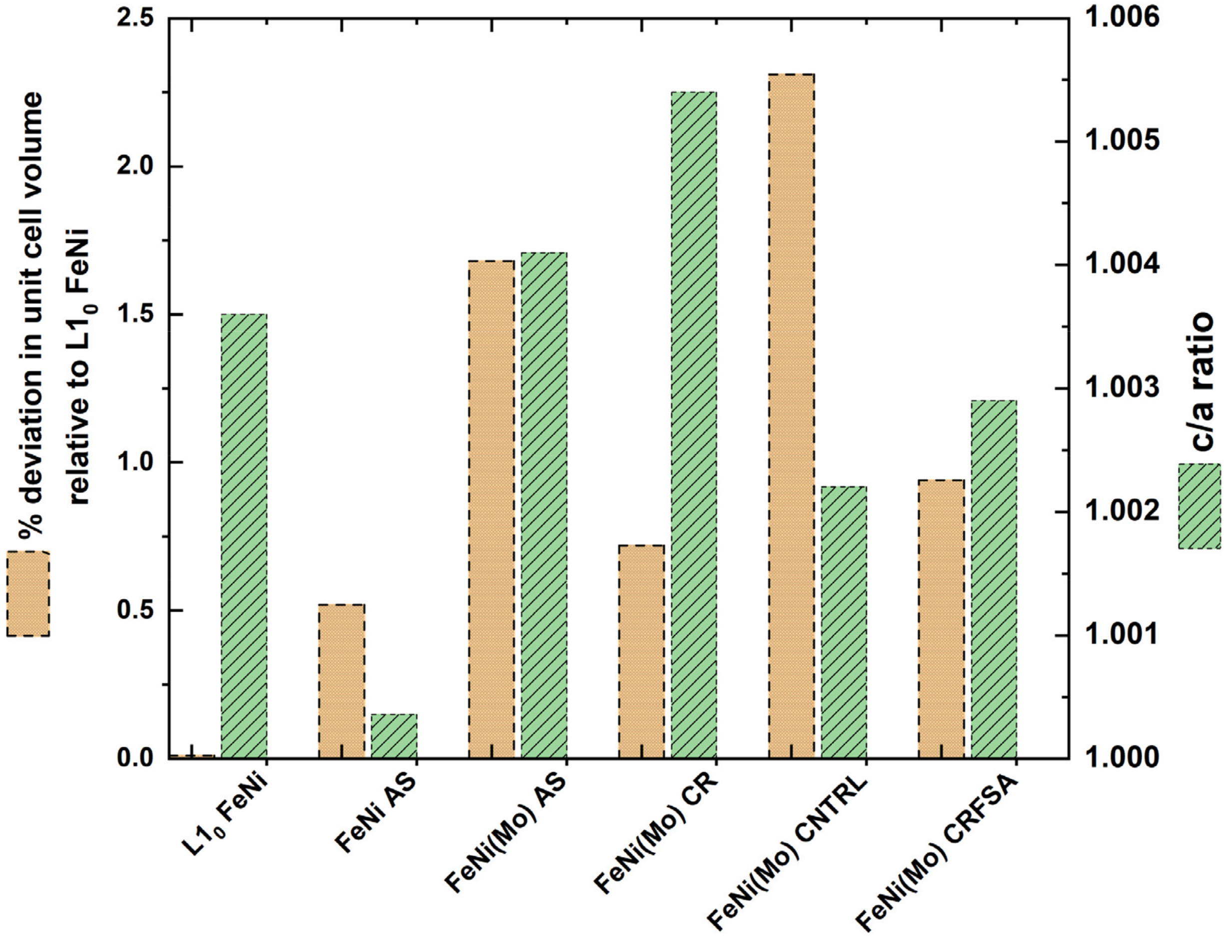

Fig. 4. Graphical display of tetragonal lattice character resulting from conventional annealing vs. MultiDriver furnace annealing, with the cold-rolled state identified as the deformed state. Comparisons relative to measured $L1_0$ values, derived from the NWA 6259 meteorite [7], of specimen unit cell deviations and *c/a* ratios as reflective of the processed state. The uncertainties associated with these data are smaller than the data markers.

resulting from the type of post-deformation annealing, either conventional annealing or versus or MultiDriver annealing, are revealing: the unit cell volume of the conventionally annealed specimen collapses precipitously from that of the precursor cold-rolled state by over 1.5%, accompanied by a strong decrease in the tetragonality ratio. In contrast, the MultiDriver CRFSA sample experiences only a very slight decrease in unit cell volume relative to the precursor deformed state, accompanied by a moderate *c/a* ratio decrease. This MultiDriver-annealed state mimics that found in the CNTRL sample and echoes the minor change in crystallographic texture noted in the CRFSA sample as compared to that found in the CNTRL sample. These results allow the conclusion that MultiDriver annealing facilitates attainment of a lattice condition in FeNi that is close to that of meteorite-derived $L1_0$ FeNi, specifically a lower unit cell volume combined with an elevated tetragonality.

4.2. Magnetic domain configurations and surface topography

Analysis of MOKE images captured from the samples of this study indicates clear differences in the magnetic domain configuration, and hence in the sample magnetic properties, induced by MultiDriver processing. Magnetic domain observation is very diagnostic and can allow detection of influences from lattice and strain distortions which are not easily visible using other techniques [73]. Basically, the character of the surface domains that are typically imaged is determined by the orientation of magnetic anisotropy axes relative to the surface. With increasing misorientation, *i.e.* misalignment between a magnetic easy axis and the sample surface, the domain complexity increases by domain branching. The character of this domain branching, on the other hand, depends on the manifold of easy axes [48]. In case of materials with cubic magnetocrystalline anisotropy, different characteristic domains are therefore expected if a surface is dominated purely by the crystal anisotropy or if lattice and strain distortions enforce an effective uniaxial anisotropy (as may be seen in Fig. 5.9 of Ref. [48]).

To better understand the effects of the processing on the magnetic properties in this study, details of the magnetic domain structure and associated surface topography of two samples are presented here: (i) a chemically unmodified FeNi as-cast (AS) sample [7] and (ii) the earlier-discussed FeNi(Mo) alloy after cold-rolling and annealing (CRFSA) in the MultiDriver Furnace. For domain interpretation it is essential to know the symmetry and magnitude of anisotropy and the quality factor Q of the material, defined as $Q = K_{\mathrm{eff}} / K_{\mathrm{d}}$, where K_{eff} is the anisotropy constant and $K_{\mathrm{d}} = J_{\mathrm{s}}^2/2\mu_0$ is the stray field coefficient (with J_{s} the saturation polarization) which is a measure of the maximum energy density that may be connected with stray fields. In materials with $Q << 1$ the magnetic stray field energy dominates the anisotropy energy; *i.e.* any magnetic anisotropy present (be it magnetocrystalline, stress-induced or of other origin) must be relatively small. It is then expected that in this case, in the zero-field state, the magnetization within the volume of the sample follows the anisotropy directions while at the sample surface the dominating stray field energy will create flux-closure domains for misoriented surfaces (*i.e.*, those sur-

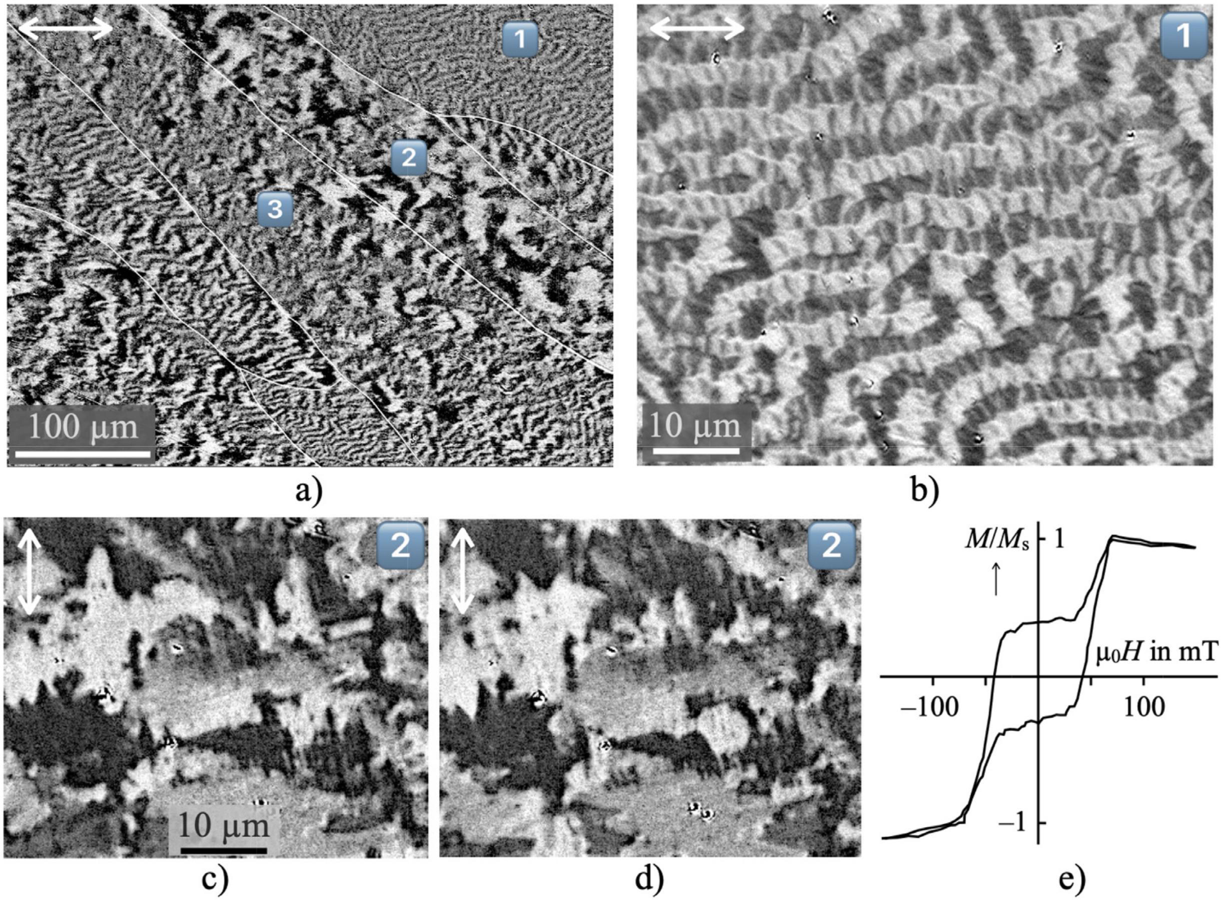

Fig. 5. Surface magnetic domain structure, observed by MOKE microscopy on the as-cast FeNi alloy. Two types of domain patterns are revealed in the overview image a) corresponding to crystallites of two different orientations as resulting from solidification. The major grain boundaries are highlighted by white lines. The high-resolution images b)–d) were taken at the indicated regions in image a). In images c) and d), two domain states at the same sample location are shown which were obtained after independent ac-field demagnetization (conditions : 10 Hz, horizontally applied magnetic field). In image e) a typical surface MOKE loop of region (2) is shown. The axes of Kerr sensitivity are marked by white arrows in the all domain images.

faces not containing an easy direction). Independent of the degree of misorientation and the domain branching, there will always be *strict* in-plane magnetization right at the surface for materials with $Q << 1$ to avoid the appearance of magnetic surface poles [48]. For comparison, high-anisotropy materials such as NdFeB or L1$_0$ FePt that typically possess quality factors $Q > 1$ may also present out-of-plane magnetization components at the surface if allowed by the anisotropy.

The *unmodified* FeNi 50 at% alloy of this study is estimated to possess a very small quality factor $Q = 0.0008$, calculated under the assumption of a saturation polarization $J_s = 1.6$ T as well as a first-order magnetocrystalline anisotropy constant $K_1 = +800$ J/m^3[74]. Typical magnetic domain patterns (in the demagnetized state) of the AS FeNi sample are shown in Fig. 5. In accordance with the positive crystal anisotropy constant value, it is expected that in this case the <100> crystal axes are the preferred directions for the magnetization. Mechanical stress, possibly frozen-in during processing, can induce anisotropies that can compete or even overcome this relatively low crystal anisotropy value by virtue of an estimated magnetostriction constant of $\lambda = +25 \times 10^{-6}$ in this material. For reasonable stress levels, however, it is not expected that such manipulation of the magnetocrystalline anisotropy will significantly change the range of the quality factor. Thus the aforementioned small Q-factor of this sample forces the magnetization polarization to lie strictly parallel to the imaged surface, independent of the orientation of the magnetic domains that are present in the underlying volume. In fact, when the domains are imaged under pure polar Kerr sensitivity conditions (data not shown), no domain contrast at all is observed. This is true for both the processed and unprocessed samples investigated in this work. All domain images, presented in the following section, were consequently obtained under pure in-plane Kerr sensitivity and the displayed domain images are representative of those found throughout the sample.

In the overview picture (Fig. 5a) numerous grains are seen with grain boundaries that follow a pronounced diagonal direction, extending from the top left corner to the bottom right corner. Two basic types of patterns can be identified: fine, stripe-like domains that resemble fingerprints (region 1 in Fig. 5a), and coarser, blocky irregular domains (region 2 in Fig. 5a). The intergrown/dendritic type region 3 shows both types of domains. Observation of the characteristic domain patterns present in the as-cast FeNi-based sample at higher resolution (Fig. 5b–d) allow a number of conclusions to be made, detailed as follows. The first conclusion is that the stripe-like domains (Fig. 5b) closely resemble branched closure domains that are typically found in amorphous ferromagnetic ribbons with the easy axis perpendicular to the ribbons' surface (compare Figs. 3.142 and 5.46 in Ref. [48]). Similar magnetic domain patterns were also observed on nickel-iron single crystals containing ~55% Ni (as seen in the previously mentioned Fig. 5.42 in Ref. [48]). The latter were attributed to stress-induced anisotropy within the crystal. Building on those observations it is concluded that the origin of the branched domain patterns shown in Fig. 5b is the presence of an effective uniaxial magnetic anisotropy with a strong component perpendicular to the as-cast specimen surface. Mechanical stress, overcoming the cubic magnetocrystalline anisotropy, may underlie this effect. Additionally, it is possible that a significant crystallographic misorientation of the surface (*i.e*. the surface does not contain easy crystal axes) contributes to the strong perpendicular component of anisotropy. The second conclusion that may be drawn from these magnetic domain images is that the multiple gray levels of Kerr contrast (Fig. 5c) found in the coarser, irregular/blocky domains of region 2 in Fig. 5a are consistent with the existence of multiple, non-collinear (effective) anisotropy axes existing at the sample surface. In this circumstance it seems that the cubic magnetocrystalline anisotropy does indeed dictate the magnetic domain pattern, possibly due to the presence of a more favorable crystallographic surface orientation. Additional MOKE examinations performed on this sample indicate that residual mechanical stress also impacts the configuration of these domains. In specific, after demagnetizing the sample in an *ac* magnetic field, the resultant zero-field domain patterns differ in detail but not in the local distribution of gray contrast level (compare Fig. 5c and d). This observation may be explained as an effect of superimposed stress-induced anisotropy, where one of the crystallographic axes is preferred relative to the others at every location in the sample. This stress-induced "fixation" of domain patterns may also underlie the typical, consistently found two-step local magnetic reversal recorded by MOKE magnetometry on all grains of this sample, exemplarily shown in Fig. 5e. Such hysteresis loops resemble the unique two-step magnetic reversal characteristic of the Perminvar effect, which was first demonstrated in a group of Fe–Ni–Co alloys[75]. Perminvar materials exhibit a constant permeability at low field strengths, together with low hysteresis losses. At a field strength less than a critical field strength, the hysteresis loop is open. With rising field strength, the loop width decreases and disappears altogether at higher magnetic field intensities. Through correlation of loop development and magnetic domain evolution in the Kerr microscope (not shown) it is confirmed that the steep parts of the recorded surface hysteresis loop are dominated by domain growth, while along the low-permeability branches the domains are pinned with very little or no wall motion. Note that the Perminvar effect is observed on the *surface* of the specimen – no conclusion is possible on the behavior of the interior volume.

In contrast, a much different magnetic domain configuration is created by MultiDriver processing. Fig. 6 shows paired topographic and magneto-optical images obtained from two separate areas that are representative of the entire CRFSA sample. The specimen is clearly inhomogenous, exhibiting a variety of significantly different magnetic domain patterns. In specific, broad (~100 μm) magnetic domains with pure black-and-white contrast are noted, separated by 180° domain walls delineating domains that are strictly magnetized in-plane. These broad magnetic domains gradually transition into mottled, micron-sized regions of gray, black and white contrast. These features are examined in more detail in Fig. 7, which also includes local magneto-optical hysteresis loops measured in three characteristic areas of the sample, denoted Areas 1–3. In Areas 2 and 3 a mottled magnetic domain pattern is present with constricted surface hysteresis loops that are very similar to the Perminvar-like loop of Fig. 5e. The high-resolution domain images in Fig. 7d the depict the above-mentioned multilevel gray domain contrast in those regions. In contrast, the very clear black-and-white wide stripes of Area 1 deliver a hysteresis loop of a very sharp and square magnetic reversal with a remanence ratio equal to unity, as expected for a loop that is governed by 180° domain wall motion. The magnetic domain boundaries are curved, following local anisotropy directions. Despite the very thorough polishing treatment applied to this sample (see Materials and Methods Section), the topographic images in Fig. 6 reveal a region of roughness that is exactly coincident with the regions containing the wide magnetic domains, consistent with local elevated mechanical hardness. In contrast, the regions that exhibit gray, mottled domain contrast are topographically very flat and smooth. As a relevant observation, within the body of meteoritic literature the $L1_0$ FeNi phase is often identified in multiphase meteorites as significantly more chemically resistant to acid etching and is notably mechanically harder than other meteoritic FeNi phases [76–79]. While the FeNi(Mo) alloy in the CNTRL state was also examined using MOKE microscopy, these images exhibited highly complex domains that resembled the domains of Area 2 in Fig. 7. These images are not included as they cannot easily be interpreted.

Summarizing, the presence of a cubic magnetocrystalline anisotropy, modified by residual stress, can be deduced from magnetic domain observations performed on the as-cast (AS) NiFe material. In contrast, large areas with uniaxial anisotropy are present in the CRFSA sample produced by MultiDriver-annealing; these uniaxial areas are interrupted by zones of very small, mottled domains that are consistent with the presence of a second phase with cubic anisotropy. Importantly, in both the as-cast and the MultiDriver-annealed material, no polar Kerr contrast could be detected; therefore the quality factor Q for the material in both processing states is not large, likely significantly smaller than unity.

5. Prospects for achieving chemical order in FeNi

Overall, all assessed parameters of FeNi alloys investigated here (crystallographic texture, unit cell volume, tetragonality ratio, magnetic domain configuration and magnetic reversal character) demonstrate consistent trends with processing, with MultiDriver processing utilizing simultaneous applied magnetic and stress fields to promote tetragonality. Conventional annealing induces an expansion of the unit cell volume and a recrystallized texture along the (200) direction while MultiDriver annealing maintains the (220) crystallographic texture of the precursor cold-rolled state and delivers lattice alterations that are in alignment with those of chemically ordered FeNi (tetrataenite): namely a lower unit cell volume and an elevated *c/a* ratio. These results permit the deduction that simultaneous application of a tensile stress and of a saturating magnetic field during annealing does indeed have an impact on the recrystallization process, in essence suppressing recovery and recrystallization to retain the alloy in its "as-deformed" state. Correspondingly, the magnetic domain images obtained from MultiDriver-processed samples show clear evidence of magnetic uniaxiality in a majority of the sample which is precisely coincident with regions of elevated mechanical hardness. While the wide, black-and-white domains of Figs. 6 and 7 are reminiscent of those found in canonically soft magnetic materials, such as silicon steels and amorphous magnetic glasses [48,80,81], the results reported here are distinguished by evidence of a very square magnetic reversal accompanied by an appreciable remanence. These attributes are consistent with magnetic uniaxiality that is accompanied by elevated magnetocrystalline anisotropy. It may thus be concluded that MultiDriver processing induces a predominant, though small, uniaxial anisotropy, which is apparently stronger than the original cubic anisotropy of the NiFe-based material.

An intriguing resemblance is noted between magnetic domains of the uniaxial regions of the MultiDriver furnace-processed FeNi sample, Figs. 6 and 7, and those exhibited by the Estherville mesosiderite meteorite containing large regions of tetrataenite, Fig. 8, as imaged by magnetic force microscopy. The Estherville meteorite fell to earth in 1879 near Estherville, Iowa, U.S.A., and remains the largest meteorite found in North America [82]. Three characteristic regions of the meteorite are identified and labeled in Fig. 8: these are the so-called Cloudy Zone (region A in the figure),

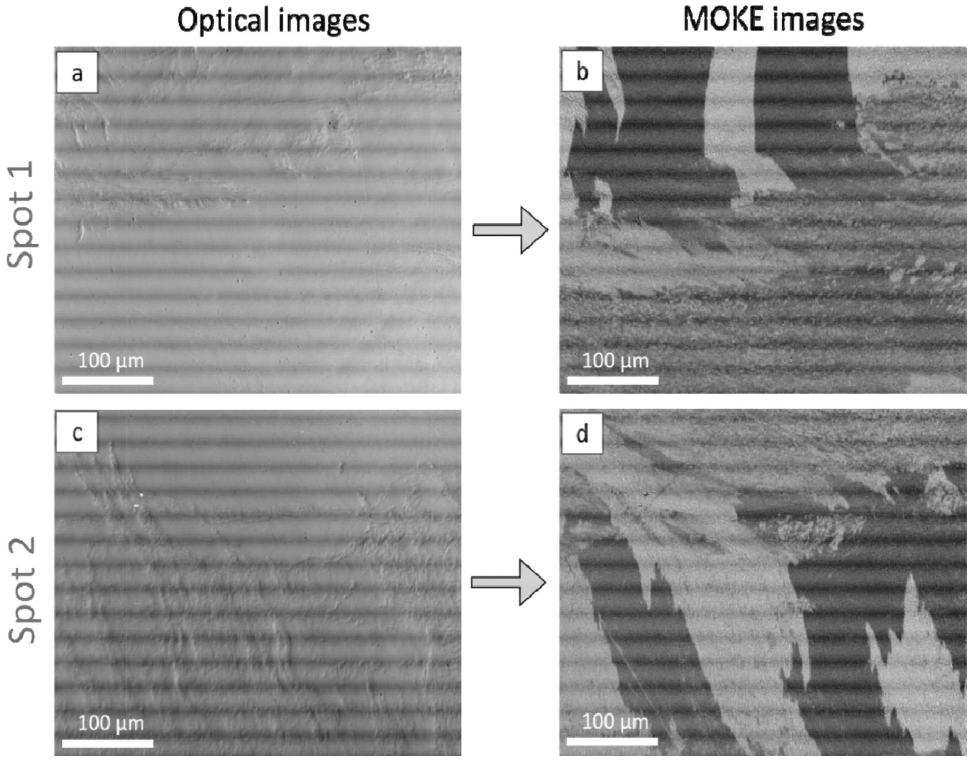

Fig. 6. Optical and MOKE images of the FeNi(Mo) CRFSA (Cold-Rolled and Field-Stress Annealed) sample. Left-hand side: surface of the samples; Right-hand side: MOKE images obtained in the demagnetized state. The Kerr sensitivity is vertical in the overview Kerr images.

which is a nanocomposite of high-Ni phases embedded in a matrix of a low-Ni phase [83,84]; kamacite (region C), an iron-based phase with the body-centered cubic (bcc) structure, and tetrataenite (region B). The tetrataenite phase imaged in Fig. 8 displays magnetic domains that are to be expected for a material with high uniaxial anisotropy [49]. All domains are strictly magnetized along the chemical ordering direction and hence are parallel to the direction of the $L1_0$ easy axis. Due to the polycrystalline microstructure in region B with grain sizes of several micrometers, the local domain appearance depends on the misalignment between the easy axis of the $L1_0$ phase and the angle of the specimen surface cut relative to the grain orientation. The flame-like appearance of the domains is due to the contrast mechanism of magnetic force microscopy which senses magnetic poles and local susceptibilities of a domain pattern [85]. The magnetic domains in Area 1 of Fig. 7 follow the same principal. Compared to those imaged in Fig. 8, however, the wide in-plane magnetized, uniaxial domains in Fig. 7 indicate the existence of an effective easy axis parallel to the surface in that region. While the strength of uniaxial anisotropy cannot be derived from the domain pattern, the similarity of parallel striped magnetic domain contrast in both types of samples is evident. This statement is supported by a comparison of Figs. 6d) and 7a, Area 1 of the processed FeNi strips with the upper right quadrant region of the Estherville meteorite, Fig. 8. It is also interesting to note the similarity between the magnetic domains of Fig. 7a), Area 3 with those of the Cloudy Zone region A, Fig. 8. This multiphase region in the Estherville meteorite consists of very fine (~2 nm diameter) particles of tetrataenite embedded in disordered FeNi [86]; under optical microscopy examination this microstructure appears cloudy after chemical etching, hence its moniker "Cloudy Zone" [87]. It is possible that the processed FeNi samples examined in this study also contain a synthesized Cloudy Zone, with confirmation left for future work. Overall, in addition to the earlier presented results, these magnetic domain comparisons provide additional evidence that the MultiDriver processing approach is of value is of value for creating favorable conditions to develop chemically ordered FeNi, on industrially relevant timescales, for technological applications.

The origin of the magnetic uniaxiality underlying the observed magnetic domain patterns and the rectangular shape of selected areas of the MultiDriver-annealed sample is attributed to the promotion of "orientational superstructures", predicted by Néel [65] and described by Chikazumi and coworkers researching $FeNi_3$ as "directional order" [66,88,89], with the latter terminology in current use. Néel claim that such a structure may be formed by rolling or stretching of polycrystalline ferronickels and is strongly related to the specific thermal recovery mechanism [90]. They attribute this effect to the tendency of nearest-neighbor atoms in ferromagnetic solid solutions annealed in a magnetic field to redistribute in an anisotropic manner around a given atom, as directed by differences in bonding between A-A, B-B and A-B atoms in a ferromagnetic binary AB solid solution. This phenomenon can give rise to an anisotropy in directional order in such alloys, which is equivalent to uniaxial anisotropy [91,92]. Supporting this framework, differences in bond lengths in FeNi alloys was investigated with synchrotron-based X-ray diffuse scattering experiments by Jiang and co-workers who measured both the local chemical order and the pairwise atomic displacements in a selection of FeNi alloys, recovering the mean static displacements for Fe–Fe, Fe–Ni and Ni–Ni pairs [93]. In the vicinity of the equiatomic composition, they found that the average Fe–Fe first-neighbor interatomic distance to be much larger than the average derived from the lattice spacing for the alloys while the Ni–Ni first-neighbor distance follows the average lattice and the Fe-Ni first-neighbor distances are smaller than average. It is concluded that these bond-length deviations from Végard's Law reflect the processing-induced creation of orientational superstructures and give rise to the tetragonality that is noted in alloys examined in this current work.

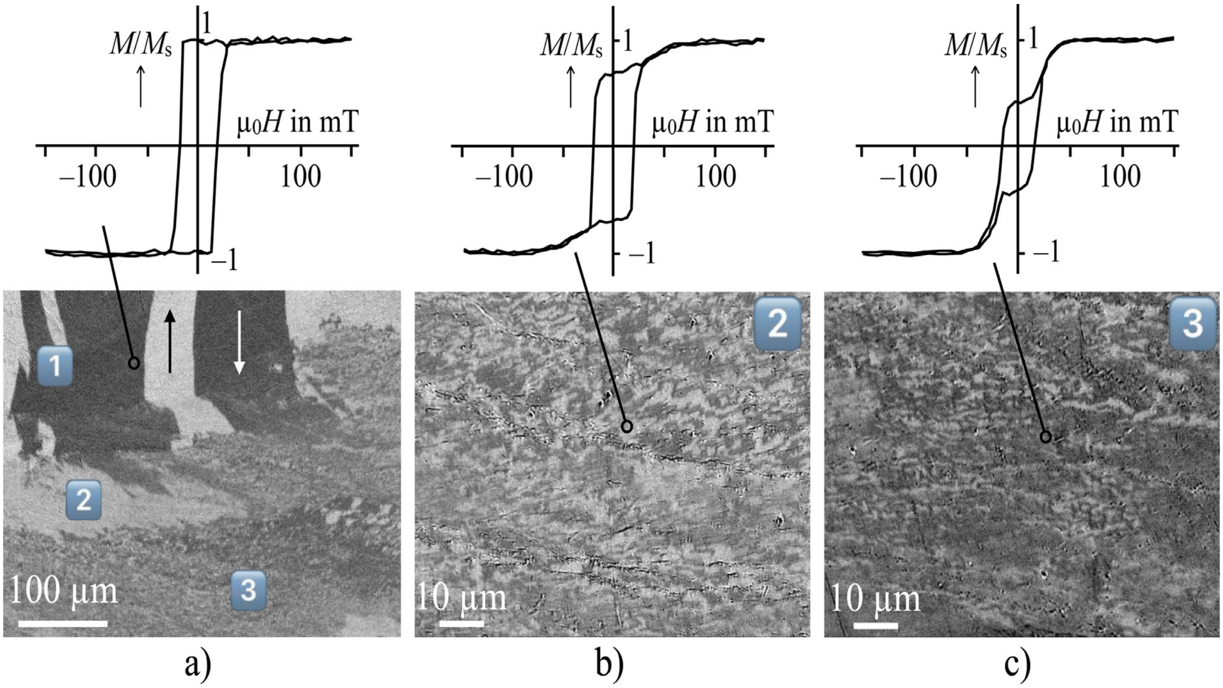

Fig. 7. MOKE images obtained in the demagnetized state of the FeNi(Mo) "CRFSA" (Cold-Rolled and Field-Stress Annealed) sample. Images b) and c) were taken under high-resolution conditions in the areas marked as 1, 2, and 3 in the low-resolution image a). The surface MOKE hysteresis loops were recorded in image spots of approximately (10 × 10) square micrometers at low resolution. All images are taken at longitudinal Kerr sensitivity. During imaging the Kerr sensitivity was along the vertical direction in all images, and the field was applied along the same axis.

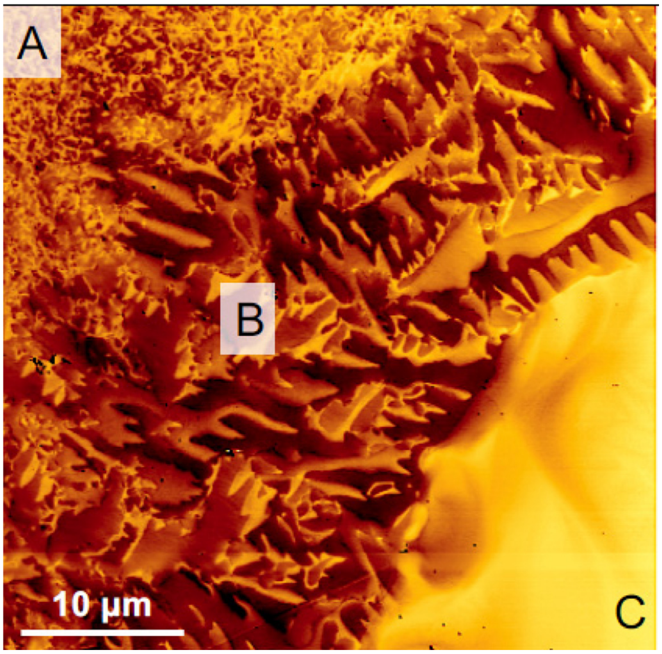

Fig. 8. Magnetic microstructure of a region of the Estherville meteorite that contains regions of the Cloudy Zone (A), tetrataenite ($L1_0$ FeNi), (B) and kamacite (bcc FeNi), (C).

The MultiDriver-processed samples demonstrate uniaxial magnetic anisotropy that is derived from induced and/or amplified lattice tetragonality. However, no evidence of chemical ordering, within the limits of detection, was obtained from the synchrotron XRD data. It is known that achievement of tetragonality is not sufficient to induce a large magnetocrystalline anisotropy in ferromagnetic binary metallic alloys. Indeed, *ab initio* electronic structure calculations conducted by Razee, Staunton and co-workers allow clarification of the relationships between magnetocrystalline anisotropy, chemical order and lattice distortion in a selection of ferromagnetic compounds [94–96]. These authors conclude that the magnetocrystalline anisotropy energies may be attributed both to lattice distortion (tetragonality) as well as to chemical ordering. In $L1_0$-type CoPt, they calculate that only about 20% of the anisotropy is furnished by adopting a non-cubic lattice, while the remaining 80% is contributed by the chemical order. This value is obviously reduced in the instance of incomplete chemical order, where the chemical order parameter *S*, which quantifies the degree that specific atomic lattice sites are occupied by specific atoms, is less than unity.

Nonetheless, prospects for attaining chemically ordered FeNi in industrially relevant timeframes remain positive. Previous work has allowed the hypothesis that the chemical ordering transformation in bulk FeNi is a two-step process: a stress-induced martensitic transformation to a tetragonal chemically disordered (A6 Strukturbericht designation) phase, followed by a diffusional process to attain the chemically ordered $L1_0$ phase [7,33]. Thus, in a sense, these current results signal partial achievement of bulk $L1_0$ FeNi. The next necessary processing step is to increase the diffusion rate in this system without a concomitant increase to high temperature. While it is known that diffusion in magnetic materials may be driven by a magnetic field gradient, literature reporting on the influence of magnetic field gradients on thermally-driven atomic diffusion in solids is both sparse and contradictory [97–99], and reports of magnetic gradient effects on first-order phase transitions in magnetoresponsive materials are not found in the literature. The dearth of literature in this area may be related to challenges of creating a large magnetic field gradient within an annealing furnace. To this end, it is proposed that MultiDriver processing may be employed to create, in a highly simple manner, a magnetic field gradient in suitably shaped samples. The effect is anticipated to be very significant, as the magnetic force is proportional to the square of the magnetic induction gradient [100,101]. It is predicted that surprisingly large magnetic field gradients can be created in the MultiDriver furnace by using specimens with a tapered geometry: for example, incorporation of a SmCo-type magnet (remanence ~0.9 T [102]) in the MultiDriver furnace can furnish a flux gradient of 90 T/m via a ten-fold reduction in area A from one end of a specimen to the other of a tapered strip of 10 cm in length. This large gradient magnitude significantly exceeds those utilized by other researchers by employing complex magnetic configurations [103,104**]**, and provides an interesting prospect for tailoring diffusional (*i.e*., thermodynamically first-order) phase transitions such as that found in FeNi.

Declaration of Competing Interest

The authors declare that they have no known competing financial interests or personal relationships that could have appeared to influence the work reported in this paper.

Acknowledgments

The authors would like to convey their sincere appreciation to Rogers Corporation, United States, the National Science Foundation (PFI:AIR-TT program Award number 1601895 and DMR-1905662) and to Northeastern University, for supporting this study. Support from the Intercountry Lectureship Program of the German-American Fulbright Commission and from Fulbright España is also gratefully acknowledged. This research used resources of the Advanced Photon Source, a U.S. Department of Energy (DOE) Office of Science User Facility operated for the DOE Office of Science by Argonne National Laboratory under Contract No. DE-AC02-06CH11357. S. Keshavarz and R. William McCallum (McCallum Consulting LLC, Santa Fe, NM, USA) contributed to the MultiDriver Furnace design and implementation, Stefan Pofahl (IFW) prepared the specimens for Kerr microscopy and Stefan Dederke (IFW) performed some confirming Kerr experiments. Special thanks to all of them.

References

[1] U.S. Application No. 62/509, 026 “Vertical Annealing Apparatus for Simultaneous Application of Stress and Magnetic Field Under an Inert Atmosphere”; Inventor(s): Laura H. Lewis, Ian J. McDonald, Sahar Keshavarz and R. William McCallum. 2017

[2] L.H. Lewis, F.E. Pinkerton, N. Bordeaux, A. Mubarok, E. Poirier, J.I. Goldstein, R. Skomski, K. Barmak, De magnete et meteorite: cosmically motivated materials, IEEE Magn. Lett. 5 (2014) 1–4, doi:10.1109/lmag.2014.2312178.

[3] P. Manchanda, P. Kumar, A. Kashyap, M.J. Lucis, J.E. Shield, A. Mubarok, J.I. Goldstein, S. Constantinides, K. Barmak, L.H. Lewis, D.J. Sellmyer, R. Skomski, Intrinsic properties of fe-substituted $L1_0$ magnets, IEEE Trans. Magn. 49 (2013) 5194–5198, doi:10.1109/tmag.2013.2261821.

[4] P. Manchanda, R. Skomski, N. Bordeaux, L.H. Lewis, A. Kashyap, Transition-metal and metalloid substitutions in $L1_0$-ordered FeNi, J. Appl. Phys. 115 (2014), doi:10.1063/1.4862722.

[[5] E. Poirier, F.E. Pinkerton, R. Kubic, R.K. Mishra, N. Bordeaux, A. Mubarok, L.H. Lewis, J.I. Goldstein, R. Skomski, K. Barmak, Intrinsic magnetic properties of $L1_0$ FeNi obtained from meteorite NWA 6259, J. Appl. Phys. 117 (2015), doi:10.1063/1.4916190.

[[6] N. Bordeaux, A. Montes-Arango, J. Liu, K. Barmak, L.H. Lewis, Thermodynamic and kinetic parameters of the chemical order–disorder transformation in $L1_0$ FeNi (tetrataenite), Acta Mater. 103 (2016) 608–615, doi:10.1016/j.actamat.2015.10.042.

[[7] A.M. Montes-Arango, L.G. Marshall, A.D. Fortes, N. Bordeaux, S. Langridge, K. Barmak, L.H. Lewis, Discovery of process-induced tetragonality in equiatomic ferromagnetic FeNi, Acta Mater. 116 (2016) 263–269, doi:10.1016/j.actamat.2016.06.050.

[8] L.H. Lewis, A. Mubarok, E. Poirier, N. Bordeaux, P. Manchanda, A. Kashyap, R. Skomski, J.I. Goldstein, F.E. Pinkerton, R.K. Mishra, Inspired by nature: investigating tetrataenite for permanent magnet applications, J. Phys.: Condensed Matter 26 (2014) 064213, doi:10.1088/0953-8984/26/6/064213.

[9] E. Stern-Taulats, T. Castán, L. Mañosa, A. Planes, N.D. Mathur, X. Moya, Multicaloric materials and effects, MRS Bull. 43 (2018) 295–299, doi:10.1557/mrs.2018.72.

[10] A. Planes, T. Castán, A. Saxena, Thermodynamics of multicaloric effects in multiferroics, Philos. Mag. 94 (2014) 1893–1908, doi:10.1080/14786435.2014.899438.

[11] Y. Liu, L.C. Phillips, R. Mattana, M. Bibes, A. Barthélémy, B. Dkhil, Large reversible caloric effect in FeRh thin films via a dual-stimulus multicaloric cycle, Nat. Commun. 7 (2016), doi:10.1038/ncomms11614.

[12] T. Gottschall, A. Gràcia-Condal, M. Fries, A. Taubel, L. Pfeuffer, L. Mañosa, A. Planes, K.P. Skokov, O. Gutfleisch, A multicaloric cooling cycle that exploits thermal hysteresis, Nat. Mater. 17 (2018) 929–934, doi:10.1038/s41563-018-0166-6.

[13] C. Koch, Experimental evidence for magnetic or electric field effects on phase transformations, Mater. Sci. Eng.: A 287 (2000) 213–218, doi:10.1016/s0921-5093(00)00778-4.

[14] Z. Sun, M. Guo, J. Vleugels, O.V.D. Biest, B. Blanpain, Strong static magnetic field processing of metallic materials: a review, Curr. Opinion Solid State Mater. Sci. 16 (2012) 254–267, doi:10.1016/j.cossms.2012.08.001.

[15] L.H. Lewis, C.H. Marrows, S. Langridge, Coupled magnetic, structural, and electronic phase transitions in FeRh, J. Phys. D Appl. Phys. 49 (2016) 323002, doi:10.1088/0022-3727/49/32/323002.

[16] R. Hamilton, H. Sehitoglu, Y. Chumlyakov, H. Maier, Stress dependence of the hysteresis in single crystal NiTi alloys, Acta Mater. 52 (2004) 3383–3402, doi:10.1016/j.actamat.2004.03.038.

[17] R. Hamilton, H. Sehitoglu, C. Efstathiou, H. Maier, Inter-martensitic transitions in Ni–Fe–Ga single crystals, Acta Mater. 55 (2007) 4867–4876, doi:10.1016/j.actamat.2007.05.003.

[18] S.N. Hsiao, F.T. Yuan, H.W. Chang, H.W. Huang, S.K. Chen, H.Y. Lee, Effect of initial stress/strain state on order-disorder transformation of FePt thin films, Appl. Phys. Lett. 94 (2009) 232505, doi:10.1063/1.3153513.

[19] H. Ohtsuka, Structural control of Fe-based alloys through diffusional solid/solid phase transformations in a high magnetic field, Sci. Technol. Adv. Mater. 9 (2008) 013004, doi:10.1088/1468-6996/9/1/013004.

[20] T. Garcin, S. Rivoirard, C. Elgoyhen, E. Beaugnon, Experimental evidence and thermodynamics analysis of high magnetic field effects on the austenite to ferrite transformation temperature in Fe–C–Mn alloys, Acta Mater. 58 (2010) 2026–2032, doi:10.1016/j.actamat.2009.11.045.

[21] H. Fujii, Effects of Magnetic-Field on Elemental Process for Microstructural Development of Iron-Based Polycrystalline Materials, Tohoku University, Japan, 2009 Doctoral Dissertation.

[22] B. Zhang, M. Lelovic, W. Soffa, The formation of polytwinned structures in Fe-Pt and Fe-Pd alloys, Scr. Metall. Mater. 25 (1991) 1577–1582, doi:10.1016/0956-716x(91)90455-a.

[23] D.E. Laughlin, K. Srinivasan, M. Tanase, L. Wang, Crystallographic aspects of $L1_0$ magnetic materials, Scr. Mater. 53 (2005) 383–388, doi:10.1016/j.scriptamat.2005.04.039.

[24] A. Kulovits, A. Deshpande, J. Wiezorek, Cold-working and annealing of the chemically ordered $L1_0$-phase Fe50–Pd50, Intermetallics 17 (2009) 865–871, doi:10.1016/j.intermet.2009.03.015.

[25] J.F. Albertsen, Tetragonal Lattice of Tetrataenite (Ordered Fe-Ni, 50-50) from 4 Meteorites, Phys. Scr. 23 (1981) 301–306, doi:10.1088/0031-8949/23/3/015.

[26] J.I. Goldstein, J.M. Short, The iron meteorites, their thermal history and parent bodies, Geochim. Cosmochim. Acta 31 (1967) 1733–1770, doi:10.1016/0016-7037(67)90120-2.

[27] C.W. Yang, D.B. Williams, J.I. Goldstein, A revision of the Fe-Ni phase diagram at low temperatures (<400 °C), J. Phase Equilib. 17 (1996) 522–531, doi:10.1007/bf02665999.

[28] J. Yang, J.I. Goldstein, Magnetic contribution to the interdiffusion coefficients in bcc (α) and fcc (γ) Fe-Ni alloys, Metall. Mater. Trans. A 35 (2004) 1681–1690, doi:10.1007/s11661-004-0077-9.

[29] Personal communication 2013, Distinguished Prof. J. I. Goldstein, U. Mass- Amherst. For information see https://en.wikipedia.org/wiki/Joseph_I._Goldstein.

[30] R. McCallum, L.H. Lewis, R. Skomski, M. Kramer, I. Anderson, Practical aspects of modern and future permanent magnets, Annu. Rev. Mater. Res. 44 (2014) 451–477, doi:10.1146/annurev-matsci-070813-113457.

[31] G. Giannopoulos, G. Barucca, A. Kaidatzis, V. Psycharis, R. Salikhov, M. Farle, E. Koutsouflakis, D. Niarchos, A. Mehta, M. Scuderi, G. Nicotra, C. Spinella, S. Laureti, G. Varvaro, L10-FeNi films on Au-Cu-Ni buffer-layer: a high-throughput combinatorial study, Sci. Rep. 8 (2018), doi:10.1038/s41598-018-34296-9.

[32] S. Goto, H. Kura, E. Watanabe, Y. Hayashi, H. Yanagihara, Y. Shimada, M. Mizuguchi, K. Takanashi, E. Kita, Synthesis of single-phase L10-FeNi magnet powder by nitrogen insertion and topotactic extraction, Sci. Rep. 7 (2017), doi:10.1038/s41598-017-13562-2.

[33] N. Vlasova, A.G. Popov, N.N. Shchegoleva, V.S. Gaviko, L.A. Stashkova, G.S. Kandaurova, D.V. Gunderov, Discovery of metastable tetragonal disordered phase upon phase transitions in the equiatomic nanostructured FePd alloy, Acta Mater. 61 (2013) 2560–2570, doi:10.1016/j.actamat.2013.01.033.

[34] Y. Kuriyama, M. Ushijima, Y. Azuma, Heat-treating furnace with Magnetic Field and Heat Treatment Method Using Same, US 6833107B2, 2004.

[35] H.H. Liebermann, N.J. Decristofaro, Ferromagnetic Amorphous Metallic Alloy and Annealing Method, WO 1998033945A1, 1998.

[36] Chunhai Du, Hailong Wang, Fengyuan Yang, P. Chris Hammel, Systematic variation of spin-orbit coupling with d-orbital filling: large inverse spin Hall effect in 3 d transition metals, Phys. Rev. B 90 (2014) 14040.

[37] A. Kulovits, J. Wiezorek, W. Soffa, W. Püschl, W. Pfeiler, The influence of deformation by cold-work on L1$_0$-ordering in anisotropic FePd, J. Alloys Compd. 378 (2004) 285–289, doi:10.1016/j.jallcom.2003.10.070.

[38] D. Setman, E. Schafler, E. Korznikova, M.J. Zehetbauer, The presence and nature of vacancy type defects in nanometals detained by severe plastic deformation, Mater. Sci. Eng.: A 493 (2008) 116–122, doi:10.1016/j.msea.2007.06.093.

[39] K. Tanaka, T. Ichitsubo, M. Koiwa, Effect of external fields on ordering of FePd, Mater. Sci. Eng.: A 312 (2001) 118–127, doi:10.1016/s0921-5093(00)01865-7.

[40] A. Montes-Arango, N. Bordeaux, J. Liu, K. Barmak, L.H. Lewis, L10 phase formation in ternary FePdNi alloys, J. Alloys Compd. 648 (2015) 845–852, doi:10.1016/j.jallcom.2015.07.019.

[41] The Materials Preparation Center, Ames Laboratory, 2020. [Online]. URL: https://www.ameslab.gov/dmse/materials-preparation-center.

[42] T. Ichitsubo, M. Nakamoto, K. Tanaka, M. Koiwa, Effect of applied stress on fcc-L10 transformation of FePd single crystal, Mater. Trans. JIM 39 (1998) 24–30, doi:10.2320/matertrans1989.39.24.

[43] K. Tanaka, T. Ichitsubo, M. Amano, M. Koiwa, K. Watanabe, Formation of mono-variant L10 structure on ordering of FePd under magnetic fields, Mater. Trans. JIM 41 (2000) 917–922, doi:10.2320/matertrans1989.41.917.

[44] 33-BM Description." 2019. [Online]. Available: https://www.aps.anl.gov/Sectors-33-34/Beamlines/33-BM.

[45] S.M. Antao, I. Hassan, J. Wang, P.L. Lee, B.H. Toby, State-of-the-art high-resolution powder X-ray diffraction (Hrpxrd) illustrated with rietveld structure refinement of quartz, sodalite, tremolite, and meionite, Can. Mineral. 46 (2008) 1501–1509, doi:10.3749/canmin.46.5.1501.

[46] I.F. Lee, T.Q. Phan, L.E. Levine, J.Z. Tischler, P.T. Geantil, Y. Huang, T.G. Langdon, M.E. Kassner, Using X-ray microbeam diffraction to study the long-range internal stresses in aluminum processed by ECAP, Acta Mater. 61 (2013) 7741–7748, doi:10.1016/j.actamat.2013.09.013.

[47] H.M. Rietveld, A profile refinement method for nuclear and magnetic structures, J. Appl. Crystallogr. 2 (1969) 65–71, doi:10.1107/s0021889869006558.

[48] B.H. Toby, R.B.V. Dreele, GSAS-II: the genesis of a modern open-source all purpose crystallography software package, J. Appl. Crystallogr. 46 (2013) 544–549, doi:10.1107/s0021889813003531.

[49] A. Hubert, R. Schäfer, Magnetic Domains. The Analysis of Magnetic Microstructures, Springer Science & Business Media, 2008.

[50] R. Schäfer, Investigation of domains and dynamics of domain walls by the magneto-optical Kerr-effect, Handbook of Magnetism and Advanced Magnetic Materials, 2007, doi:10.1002/9780470022184.hmm310.

[51] I.V. Soldatov, R. Schäfer, Advanced MOKE magnetometry in wide-field Kerr-microscopy, J. Appl. Phys. 122 (2017) 153906, doi:10.1063/1.5003719.

[52] W. Kuch, R. Schäfer, P. Fischer, F. Hillebrecht, Magnetic Microscopy of Layered Structures, Springer, Berlin Heidelberg, 2015.

[53] B.L. Bramfitt, A.O. Benscoter, Metallographer's guide: practice and procedures for irons and steels, ASM Int. Chapters 7 and 8 (2002).

[54] G. Petzow, J. Back, T. Mager, A. Schrader, Metallographisches Ätzen, Borntraeger 1 (1976).

[55] C. Mudivarthi, S.-.M. Na, R. Schaefer, M. Laver, M. Wuttig, A.B. Flatau, Magnetic domain observations in Fe–Ga alloys, J. Magn. Magn. Mater. 322 (2010) 2023–2026, doi:10.1016/j.jmmm.2010.01.027.

[56] V. Hoffmann, R. Schäfer, E. Appel, A. Hubert, H. Soffel, First domain observations with the magneto-optical Kerr effect on Ti-ferrites in rocks and their synthetic equivalents, J. Magn. Magn. Mater. 71 (1987) 90–94, doi:10.1016/0304-8853(87)90336-2.

[57] I.V. Soldatov, R. Schäfer, Selective sensitivity in Kerr microscopy, Rev. Sci. Instrum. 88 (2017) 073701, doi:10.1063/1.4991820.

[58] B.D. Cullity, S.R. Stock, Elements of X-ray Diffraction, third ed., Pearson Education, 2014.

[59] S. Dubois, J. Colin, J.L. Duvail, L. Piraux, Evidence for strong magnetoelastic effects in Ni nanowires embedded in polycarbonate membranes, Phys. Rev. B 61 (2000) 14315–14318, doi:10.1103/physrevb.61.14315.

[60] G. Kartopu, O. Yalçın, K.-.L. Choy, R. Topkaya, S. Kazan, B. Aktaş, Size effects and origin of easy-axis in nickel nanowire arrays, J. Appl. Phys. 109 (2011) 033909, doi:10.1063/1.3531565.

[61] P.V. Yekta, A. Ghasemi, E.M. Sharifi, Magnetic and mechanical properties of cold-rolled permalloy, J. Magn. Magn. Mater. 468 (2018) 155–163, doi:10.1016/j.jmmm.2018.07.088.

[62] S. Zaefferer, T. Baudin, R. Penelle, A study on the formation mechanisms of the cube recrystallization texture in cold rolled Fe–36%Ni alloys, Acta Mater. 49 (2001) 1105–1122, doi:10.1016/s1359-6454(00)00387-6.

[63] W.E. Seymour, D. Harker, Recrystallization reaction kinetics and texture studies of a 50 iron 50 nickel alloy, JOM 2 (1950) 1001–1004, doi:10.1007/bf03399097.

[64] 阿部秀夫, 関文男, 50% Fe-Ni 合金圧延板の再結晶集合組織, 日本金属学会誌. 23 (1959) 343–347

[65] B.H. Toby, R factors in Rietveld analysis: how good is good enough? Powder Diffr. 21 (2006) 67–70, doi:10.1154/1.2179804.

[66] R.J. Wakelin, E.L. Yates, A study of the order-disorder transformation in iron-nickel alloys in the region FeNi$_3$, Proc. Phys. Soc. Sect. B 66 (1953) 221–240, doi:10.1088/0370-1301/66/3/310.

[67] B. Predel, in: Fe-Ni (Iron-Nickel). in Dy-Er-Fr-Mo, Springer, Berlin, Heidelberg, 1995, pp. 1–12.

[68] C. Liang, C. Gooneratne, Q. Wang, Y. Liu, Y. Gianchandani, J. Kosel, Magnetic properties of FeNi-based thin film materials with different additives, Biosensors 4 (2014) 189–203, doi:10.3390/bios4030189.

[69] T. Myslowicki, T.E. Weirich, W. Bleck, Contraction of high strength Invar steel during creep test, Steel Res. Int. 74 (2003) 376–385, doi:10.1002/srin.200300201.

[70] W. Pepperhoff, Physical properties, in: V.D. Eisenhüttenleute (Ed.), Steel: Fundamentals v.1: A Handbook for Materials Research and Engineering, Springer, Berlin, Germany, 1992.

[71] P.V. Yekta, A. Ghasemi, E.M. Sharifi, Magnetic and mechanical properties of cold-rolled permalloy, J. Magn. Magn. Mater. 468 (2018) 155–163, doi:10.1016/j.jmmm.2018.07.088.

[72] A.M.M. Arango, Understanding Chemical Ordering in Near-Equiatomic Bulk FePd, FeNi, and Related Ternary Alloys, Northeastern University, 2016 Doctoral dissertation.

[73] L. Néel, Anisotropie magnétique superficielle et surstructures dorientation, J. Phys. Radium 15 (1954) 225–239, doi:10.1051/jphysrad:01954001504022500.

[74] R. Hilzinger, W. Rodewald, Magnetic Materials, Fundamentals, Products, Properties, Applications, Publicis Publishing, Erlangen, 2013.

[75] H.J. Williams, M. Goertz, Domain structure of perminvar having a rectangular hysteresis loop, J. Appl. Phys. 23 (1952) 316–323, doi:10.1063/1.1702200.

[76] E.V. Brusnitsyna, V.I. Grokhovsky, M.G. Minin, Nanoindentation of different structures within the metallic part of the seymchan pallasite PMG, in: Proceedings of 79th Annual Meeting of the Meteoritical Society, 1921, 2016.

[77] E.R.D. Scott, G.J. Taylor, A.N. Krot, Links between terrestrial planets and chondrites, Meteor. Planet. Sci. Suppl. 36 (2001) A185.

[78] E. Dos Santos, J. Gattacceca, P. Rochette, G. Fillion, R. Scorzelli, Kinetics of tetrataenite disordering, J. Magn. Magn. Mater. 375 (2015) 234–241, doi:10.1016/j.jmmm.2014.09.051.

[79] R.B. Scorzelli, I. Souza Azevedo, Mössbauer Spectroscopic Studies on Mesosiderites, Meteor. Planet. Sci. Suppl. 36 (2001) A185.

[80] T. Egami, P.J. Flanders, C.D. Graham, Low−field magnetic properties of ferromagnetic amorphous alloys, Appl. Phys. Lett. 26 (1975) 128–130, doi:10.1063/1.88072.

[81] J.D. Livingston, W. Morris, T. Jagielinski, Effects of anisotropy on domain structures in amorphous ribbons, IEEE Trans. Magn. 19 (1983) 1916–1918, doi:10.1109/tmag.1983.1062626.

[82] R.S. Clarke, E.R.D. Scott, Tetrataenite-ordered FeNi, a new mineral in meteorites, Am. Mineral. 65 (1980) 624–630.

[83] C.W. Yang, D.B. Williams, J.I. Goldstein, A new empirical cooling rate indicator for meteorites based on the size of the cloudy zone of the metallic phases, Meteorit. Planet Sci. 32 (1997) 423–429, doi:10.1111/j.1945-5100.1997.tb01285.x.

[84] J.F. Einsle, A.S. Eggeman, B.H. Martineau, Z. Saghi, S.M. Collins, R. Blukis, P.A.J. Bagot, P.A. Midgley, R.J. Harrison, Nanomagnetic properties of the meteorite cloudy zone, Proc. Natl. Acad. Sci. 115 (2018), doi:10.1073/pnas.1809378115.

[85] E. Zueco, W. Rave, R. Schäfer, A. Hubert, L. Schultz, Combined Kerr-/magnetic force microscopy on NdFeB crystals of different crystallographic orientation, J. Magn. Magn. Mater. 190 (1–2) (1998) 42–47.

[86] P. Novotny, Tetrataenite in the Estherville mesosiderite, Meteoritics 16 (1981) 370.

[87] K.B. Reuter, D.B. Williams, J.I. Goldstein, Microanalysis and microdiffraction of two-phase regions in the metallic phase of the Estherville meteorite, in: Analytical Electron Microscopy, San Francisco Press, 1984, pp. 177–182.

[88] L. Néel, Anisotropie magnétique superficielle et surstructures dorientation, J. Phys. Radium 15 (1954) 225–239, doi:10.1051/jphysrad:01954001504022500.

[89] S. Chikazumi, K. Suzuki, H. Iwata, Studies on the magnetic anisotropy induced by cold rolling of ferromagnetic crystal (I) iron-nickel alloys, J. Phys. Soc. Jpn. 12 (1957) 1259–1276, doi:10.1143/jpsj.12.1259.

[90] L. Neel, Surface magnetic anisotropy and orientational superlattices, in: N. Kurti (Ed.), Selected Works of Louis Neel, CRC Press, 1988.

[91] G. Rathenau, J. Snoek, Magnetic anisotropy phenomena in cold rolled nickel-iron, Physica 8 (1941) 555–575, doi:10.1016/s0031-8914(41)80037-8.

[92] E.T. Ferguson, Uniaxial magnetic anisotropy induced in Fe–Ni alloys by magnetic anneal, J. Appl. Phys. 29 (1958) 252–253, doi:10.1063/1.1723093.

[93] X. Jiang, G.E. Ice, C.J. Sparks, L. Robertson, P. Zschack, Local atomic order and individual pair displacements of Fe$_{46.5}$Ni$_{53.5}$ and Fe$_{22.5}$Ni$_{77.5}$ from diffuse x-ray scattering studies, Phys. Rev. B 54 (1996) 3211–3226, doi:10.1103/physrevb.54.3211.

[94] J.B. Staunton, S. Ostanin, S.S.A. Razee, B. Gyorffy, L. Szunyogh, B. Ginatempo, E. Bruno, Long-range chemical order effects upon the magnetic anisotropy of FePt alloys from anab initioelectronic structure theory, J. Phys.: Condensed Matter 16 (2004), doi:10.1088/0953-8984/16/48/019.

[95] S.S.A. Razee, J.B. Staunton, B. Ginatempo, E. Bruno, F.J. Pinski, Ab initiotheoretical description of the dependence of magnetocrystalline anisotropy on both compositional order and lattice distortion in transition metal alloys, Phys. Rev. B 64 (2001), doi:10.1103/physrevb.64.014411.

[96] S.S.A. Razee, J.B. Staunton, D.D. Johnson, B. Ginatempo, E. Bruno, Correlation of magnetocrystalline anisotropy of Fe$_{0.5}$Pd$_{0.5}$ alloy with chemical order, J. Phys.: Condensed Matter 13 (2001) 8153–8160, doi:10.1088/0953-8984/13/35/320.

[97] W.V. Youdelis, D.R. Colton, J. Cahoon, On the theory of diffusion in a magnetic field, Can. J. Phys. 42 (1964) 2217–2237, doi:10.1111/j.1365-246X.1975.tb01615.x.

[98] S. Nakamichi, S. Tsurekawa, Y. Morizono, T. Watanabe, M. Nishida, A. Chiba, Diffusion of carbon and titanium in γ -iron in a magnetic field and a magnetic field gradient, J. Mater. Sci. 40 (2005) 3191–3198, doi:10.1007/s10853-005-2683-3.

[99] H. Nakajima, S. Maekawa, Y. Aoki, M. Koiwa, Diffusion of nickel in titanium in a magnetic field, Trans. Jpn. Inst. Metals 26 (1985) 1–6, doi:10.2320/matertrans1960.26.1.

[100] B.D. Plouffe, L.H. Lewis, S.K. Murthy, Computational design optimization for microfluidic magnetophoresis, Biomicrofluidics 5 (2011) 013413, doi:10.1063/1.3553239.

[101] B.D. Plouffe, S.K. Murthy, L.H. Lewis, Fundamentals and application of magnetic particles in cell isolation and enrichment: a review, Rep. Prog. Phys. 78 (2014) 016601, doi:10.1088/0034-4885/78/1/016601.1.

[102] K.J. Strnat, Handbook of Ferromagnetic Materials, North Holland, 1988, pp. 131–209. (Eds.).

[103] S. Nakamichi, S. Tsurekawa, Y. Morizono, T. Watanabe, M. Nishida, A. Chiba, Diffusion of carbon and titanium in γ -iron in a magnetic field and a magnetic field gradient, J. Mater. Sci. 40 (2005) 3191–3198, doi:10.1007/s10853-005-2683-3.

[104] A. Perigo, R.V. Martin, Magnetic Field, Gradient standards using permanent magnets: design considerations, construction and validation by nuclear magnetic resonance, IEEE Trans. Magn. 49 (2013) 4717–4720, doi:10.1109/tmag.2013.2255866.